

Carrier Aggregation Enabled MIMO-OFDM Integrated Sensing and Communication

Haotian Liu, *Student Member, IEEE*, Zhiqing Wei, *Member, IEEE*, Jinghui Piao, Huici Wu, *Member, IEEE*, Xingwang Li, *Senior Member, IEEE*, Zhiyong Feng, *Senior Member, IEEE*

Abstract—In the evolution towards the forthcoming era of sixth-generation (6G) mobile communication systems characterized by ubiquitous intelligence, integrated sensing and communication (ISAC) is in a phase of burgeoning development. However, the capabilities of communication and sensing within single frequency band fall short of meeting the escalating demands. To this end, this paper introduces a carrier aggregation (CA)-enabled multi-input multi-output orthogonal frequency division multiplexing (MIMO-OFDM) ISAC system fusing the sensing data on high and low-frequency bands by symbol-level fusion for ultimate communication experience and high-accuracy sensing. The challenges in sensing signal processing introduced by CA include the initial phase misalignment of the echo signals on high and low-frequency bands due to attenuation and radar cross section, and the fusion of the sensing data on high and low-frequency bands with different physical-layer parameters. To this end, the sensing signal processing is decomposed into two stages. In the first stage, the problem of initial phase misalignment of the echo signals on high and low-frequency bands is solved by the angle compensation, space-domain diversity and vector cross-correlation operations. In the second stage, this paper realizes symbol-level fusion of the sensing data on high and low-frequency bands through sensing vector rearrangement and cyclic prefix adjustment operations, thereby obtaining high-precision sensing performance. Then, the closed-form communication mutual information (MI) and sensing Cramér-Rao lower bound (CRLB) for the proposed ISAC system are derived to explore the theoretical performance bound with CA. Simulation results validate the feasibility and superiority of the proposed ISAC system.

Index Terms—Carrier aggregation (CA), integrated sensing and communication (ISAC), multi-band cooperative ISAC, multi-input multi-output (MIMO), orthogonal frequency division multiplexing (OFDM).

I. INTRODUCTION

The next-generation mobile communication system is anticipated to offer a plethora of multi-dimensional services extending beyond mere communication, such as smart transportation, smart factories, and digital twins [1], which have raised the demands for high-speed communication and high-accuracy sensing. To this end, integrated sensing and communication (ISAC) is considered to provide the high-speed communication experience and high-accuracy sensing [2]–[5].

Nevertheless, the limitations imposed by sensing under single frequency band have spurred the study of ISAC over

multiple frequency bands with the technique of carrier aggregation (CA). CA-enabled ISAC systems have the following potential advantages.

- **Communication:** CA enhances bandwidth utilization and boosts communication transmission data rate while supporting various wireless access technologies, thereby improving overall communication performance [6].
- **Sensing:** CA empowers sensing systems with expanded bandwidth, which facilitates high-resolution sensing and anti-noise performance [5], [7].

Therefore, it is reasonable to utilize CA to empower ISAC mobile communication system, which is expected to bring expeditious communication and precision sensing.

The researches on CA-enabled ISAC systems are classified into two types: intra-band CA and inter-band CA. The main challenges of CA-enabled ISAC system lie in signal design and processing. A summary of the related work is shown in Table I and the details are as follows.

- **Intra-band CA:** Two primary ISAC signals are designed for intra-band CA: steeped-carrier OFDM ISAC signal and non-continuous (NC) fragmented OFDM ISAC signals. In terms of steeped-carrier OFDM ISAC signals, Pfeffer *et al.* [8] proposed the concept of steeped-carrier OFDM signals, which assigns different carrier frequencies to each resource block group during the continuous OFDM symbol times, expanding the overall bandwidth and enhancing the sensing performance. However, it fails to consider the Doppler frequency shift induced by rapidly moving targets. To this end, Schweizer *et al.* [9] explored a modified DFT method to mitigate the phase error caused by the high mobility of targets in steeped-carrier OFDM scheme, which obtains a high-accuracy velocity estimation. In terms of NC fragmented OFDM ISAC signals, Huang *et al.* [10] introduced a NC fragmented OFDM ISAC system, which can flexibly allocate spectrum bands and adapt to dynamic spectrum environment. However, the missing spectrum bands deteriorate Fourier sidelobes in target sensing. To address this problem, Liu *et al.* [11] proposed a joint compressed sensing (CS) and machine learning sensing method for fragmented spectrum bands to achieve high-accuracy estimation of range and velocity with low sidelobes.
- **Inter-band CA:** Multi-band radar stands as a representative example in inter-band CA. Cuomo [12] discussed a NC multi-band coherent radar and proposed a bandwidth extrapolation (BWE) method to recover missing

Haotian Liu, Zhiqing Wei, Jinghui Piao, Huici Wu, Zhiyong Feng are with the Beijing University of Posts and Telecommunications, Beijing 100876, China (emails: {haotian_liu; weizhiqing; piaojinghui; dailywu; fengzy}@bupt.edu.cn). Correspond authors: Zhiqing Wei, Haotian Liu.

Xingwang Li is with the Henan Polytechnic University, Jiaozuo 454000, China (e-mail: lixingwangbupt@gmail.com).

TABLE I: A summary for the related work, with the abbreviations OFDM: orthogonal frequency division multiplexing, DFT: discrete Fourier transmit, CS: compressed sensing, NC: non-continuous, BWE: bandwidth extrapolation.

Types	related work	Innovation	Shortcoming
Intra-band CA	[8]	Introducing the concept of steeped-carrier OFDM radar to achieve high-resolution sensing	Only suitable for low speed targets
	[9]	Proposing a novel DFT method to address the shortcoming in [8]	Poor anti-noise performance
	[10]	An ISAC system under NC fragmented spectrum bands is proposed to enhance spectrum utilization	The degradation of Fourier sidelobes
	[11]	A CS-based sensing method is proposed to overcome the shortcoming in [10]	High computational complexity
Inter-band CA	[12]	A BWE method is proposed to recovery the data on missing spectrum bands	The resolution performance is limited
	[13]	Extending the BWE method to polarimetric radar results in a higher enhancement in resolution	Unsuitable for OFDM signal
	[7]	Joint high and low-frequency bands OFDM signal for high-accuracy sensing	Unsuitable for multiple antennas system

spectrum bands, thereby enhancing the range resolution of radar. Suwa *et al.* [13] extended the BWE method to polarimetric radar, which achieves high resolution of range estimation.

In summary, intra-band and inter-band CA enhance the efficient utilization of fragmented spectrum bands, leading to performance gains in both communication and sensing. Currently, the fragmented spectrum bands in mobile communication system are mostly dispersed, indicating broader applications in mobile communication system under inter-band CA. However, the investigation into inter-band CA in ISAC mobile communication systems is notably scarce. In our previous work, we have investigated the CA-enabled OFDM ISAC system, corroborating the effectiveness of CA through the validation [7]. However, our initial exploration, although valuable, remains somewhat rudimentary and idealized, overlooking the typical MIMO-OFDM signal in mobile communication systems.

Hence, this paper investigates a CA-enabled MIMO-OFDM ISAC system where the fragmented high and low-frequency bands are shared for downlink (DL) communication and potential target sensing. In addition, a CA-enabled MIMO-OFDM ISAC signal model and the corresponding sensing processing method are presented. Through theoretical derivations and numerical simulations, we validate the superiority of the proposed ISAC system over conventional ISAC systems. The main contributions of this paper are summarized as follows.

- We present a CA-enabled MIMO-OFDM ISAC system aiming at achieving unparalleled communication experience and high-accuracy sensing. By introducing CA and MIMO, the communication capacity of ISAC system is significantly enhanced, as well as improving the accuracy and anti-noise capability of sensing. The simulation results validate the feasibility and efficiency of the proposed ISAC system, demonstrating its advantages over conventional ISAC systems.
- In terms of sensing processing, we have delved into the data-level and symbol-level fusion of the sensing data on high and low-frequency bands. In the symbol-level fusion of sensing data, two challenges manifest: 1) The initial phase misalignment of the echo signals on high

and low-frequency bands due to attenuation and radar cross section (RCS); 2) The fusion of the sensing data on high and low-frequency bands with different physical-layer parameters. To this end, this paper decomposes the sensing signal processing into signal preprocessing stage and sensing information fusion stage. The signal preprocessing stage fully leverage the sensing data from multiple antennas while aligning the initial phases of the echo signals on high and low-frequency bands using the cyclic cross-correlation (CCC) method, as detailed in Section III-A. In the sensing information fusion stage, this paper realizes the symbol-level fusion of the sensing data on high and low-frequency bands, as well as the range and velocity estimations of target by rearranging the high and low-frequency feature vectors and using the premise of cyclic prefix (CP) dynamic adjustment, as detailed in Section III-B.

- The theoretical boundaries of the proposed CA-enabled MIMO-OFDM ISAC signal are derived. Specifically, mutual information (MI) is adopted as the performance metric for communication, while the Cramér-Rao lower bound (CRLB) is utilized as a typical performance metric of sensing. Based on the proposed ISAC system, we derived the closed-form communication MI under the frequency-selective fading MIMO-OFDM channel model and sensing CRLBs for range and velocity estimations under the MIMO-OFDM sensing signal model.

The rest of the paper is organized as follows. Section II introduces the system model, including the communication model and sensing model. In Section III, a novel CA-enabled MIMO-OFDM ISAC signal processing method is proposed. Section IV derives the communication MI and sensing CRLB of the proposed CA-enabled MIMO-OFDM ISAC signal. The simulation results are provided in Section V, while the conclusions are outlined in Section VI.

Notations: $\{\cdot\}$ typically stands for a set of various index values. Black bold letters represent matrices or vectors. \mathbb{C} and \mathbb{R} denote the set of complex and real numbers, respectively. $[\cdot]^T$, $[\cdot]^H$, and $(\cdot)^*$ stand for the transpose operator, conjugate transpose operator, and conjugate operator, respectively. For a complex-valued vector \mathbf{u} , $\text{diag}(\mathbf{u})$ stands for a diagonal

matrix whose diagonal elements are given by the elements of \mathbf{u} . $\det(\mathbf{u})$ and $\text{tr}(\mathbf{u})$ are the determinant and trace of \mathbf{u} , respectively. $E(\cdot)$ stands for the expectation operator. A complex Gaussian random variable \mathbf{u} with mean μ_u and variance σ_u^2 is denoted by $\mathbf{u} \sim \mathcal{CN}(\mu_u, \sigma_u^2)$. \circ is the Hadamard product.

II. SYSTEM MODEL

We consider a CA-enabled MIMO-OFDM ISAC base station (BS) for DL communication and target sensing as shown in Fig. 1. The ISAC BS is equipped with $N_T + N_R$ antennas, where N_T transmit antennas in transmitter (Tx) simultaneously serve U user equipments (UEs) with N_U antennas and detect potential targets. N_R receive antennas in receiver (Rx) are equipped to receive the echo signals reflected by targets [14]. The spacing of antennas in BS is denoted by d_T [15].

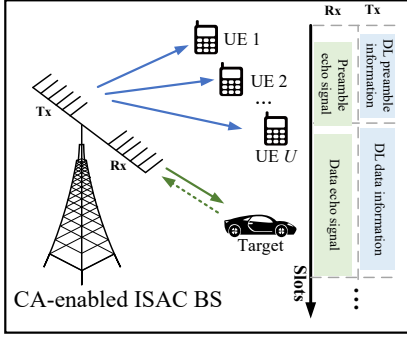


Fig. 1: CA-enabled MIMO-OFDM ISAC system.

A. CA-enabled MIMO-OFDM ISAC Signal

For the $b \in \mathcal{B} = \{1, 2\}$ -th carrier component (CC) of the ISAC BS, a total number of N_b subcarriers and M_b OFDM symbols are used for DL communication and sensing, where $n \in \{0, 1, \dots, N_b - 1\}$ and $m \in \{0, 1, \dots, M_b - 1\}$ denote the indices of subcarriers and OFDM symbols, respectively. For the b -th CC, the symbol data matrix [16]

$$\mathbf{S}^b = [\mathbf{S}_0^b, \mathbf{S}_1^b, \dots, \mathbf{S}_{N_b-1}^b]^T \in \mathbb{C}^{U N_b \times M_b} \quad (1)$$

represents the data for all UEs on N_b subcarriers during M_b OFDM symbol times, where $\mathbf{S}_n^b = [s_{n,1}^b, s_{n,2}^b, \dots, s_{n,U}^b] \in \mathbb{C}^{M_b \times U}$ indicates the data for all UEs on the n -th subcarrier during M_b symbol times with $s_{n,u}^b \in \mathbb{C}^{M_b \times 1}$ being the specific symbol data vector for the $u \in \{1, 2, \dots, U\}$ -th UE [16]. To guarantee that the communication beam focuses on UEs and potential targets, the symbol data matrix undergoes a precoding operation [17]. Specifically, a compact precoding matrix [16]

$$\mathbf{W}^b = \text{diag}(\mathbf{W}_0^b, \mathbf{W}_1^b, \dots, \mathbf{W}_{N_b-1}^b) \in \mathbb{C}^{N_b N_T \times N_b U} \quad (2)$$

is designed for all UEs on N_b subcarriers. $\mathbf{W}_n^b = [\mathbf{w}_{n,1}^b, \mathbf{w}_{n,2}^b, \dots, \mathbf{w}_{n,U}^b] \in \mathbb{C}^{N_T \times U}$ denotes the precoding matrix for all UEs on the n -th subcarriers with $\mathbf{w}_{n,u}^b \in \mathbb{C}^{N_T \times 1}$ being the specific precoding vector for the u -th UE [16].

Therefore, the transmit precoded data on N_b subcarriers during M_b symbol times is [16]

$$\begin{aligned} \mathbf{X}^b &= \mathbf{W}^b \mathbf{S}^b \\ &= [(\mathbf{X}_0^b)^T, (\mathbf{X}_1^b)^T, \dots, (\mathbf{X}_{N_b-1}^b)^T]^T \in \mathbb{C}^{N_b N_T \times M_b}, \end{aligned} \quad (3)$$

where $\mathbf{X}_n^b = \mathbf{W}^b (\mathbf{S}_n^b)^T \in \mathbb{C}^{N_T \times M_b}$ is the data on the n -th subcarrier during M_b OFDM symbol times. The transmit precoded data is transformed into time-domain signal by undergoing an inverse discrete Fourier transform (IDFT).

Therefore, the baseband time-domain transmit signal by the k -th transmit antenna on the n' -th subcarrier during the m -th OFDM symbol time in the b -th CC is [18]

$$x^b(k, n', m) = \frac{1}{N_b} \sum_{n=0}^{N_b-1} \mathbf{X}_n^b(k, m) e^{j2\pi \frac{n'n}{N_b}}, \quad (4)$$

where $\mathbf{X}_n^b(k, m)$ denotes the (k, m) -th element of \mathbf{X}_n^b , $n' \in \{0, 1, \dots, N_b - 1\}$ represents the index of subcarriers in time-domain and $k \in \{0, 1, \dots, N_T - 1\}$ represents the index of transmit antenna. A CP with size N_s^b greater than the maximum delay caused by target reflection is added to avoid inter-symbol interference. After digital-to-analog conversion (DAC), the analog signals of the 1-st and 2-nd CCs are up-converted using different local oscillators (LOs), mixed, and transmitted via a high power amplifier (HPA).

Overall, the CA-enabled MIMO-OFDM ISAC signal by the k -th transmit antenna on the n -th subcarrier during the m -th OFDM symbol time is expressed as

$$x(t)_k = \sum_{b=1}^{\mathcal{B}} \sum_{m=0}^{M_b-1} \sum_{n=0}^{N_b-1} \mathbf{X}_n^b(k, m) e^{j2\pi t(f_C^b + n\Delta f^b)} \text{rect}\left(\frac{t - mT^b}{T^b}\right), \quad (5)$$

where f_C^b denotes the carrier frequency of the b -th CC; $\Delta f^b = 1/T_{\text{ofdm}}^b$ is the subcarrier spacing of the b -th CC, where T_{ofdm}^b is the elementary symbol duration [18]; $T^b = T_{\text{ofdm}}^b + T_s^b$ is the total symbol duration with $T_s^b = (N_s^b T_{\text{ofdm}}^b)/N_b$ being an adjustable CP duration.

B. Communication Model

In the communication channel model, the differences in attenuations caused by high and low-frequency bands are not considered.

1) *Communication channel model*: We utilize the widely adopted multi-path channel model in MIMO channels, assuming the presence of L delay paths in the communication environment. The index of receive antennas in UE is denoted by $z \in \{0, 1, \dots, N_U - 1\}$ and

$$\mathbf{H}_u^{l,b} = \begin{bmatrix} h_{0,0}^{u,l,b} & h_{0,1}^{u,l,b} & \dots & h_{0,N_U-1}^{u,l,b} \\ h_{1,0}^{u,l,b} & h_{1,1}^{u,l,b} & \dots & h_{1,N_U-1}^{u,l,b} \\ \vdots & \vdots & \ddots & \vdots \\ h_{N_T-1,0}^{u,l,b} & h_{N_T-1,1}^{u,l,b} & \dots & h_{N_T-1,N_U-1}^{u,l,b} \end{bmatrix} \in \mathbb{C}^{N_T \times N_U} \quad (6)$$

is the channel matrix of the $l \in \{0, 1, \dots, L - 1\}$ -th delay path for the u -th UE with $h_{k,z}^{u,l,b} \sim \mathcal{CN}(0, 1)$ being the corresponding channel element with independent identically distributed (i.i.d.) Rayleigh fading coefficients [16]. Therefore, the MIMO communication channel matrix in time-domain for

the u -th UE on the n -th subcarrier during the m -th OFDM symbol time is expressed as [18]

$$\mathbf{H}_{u,m}^n = \sum_{l=0}^{L-1} \mathbf{H}_u^{l,b} \delta[m-l] \in \mathbb{C}^{N_T \times N_U}. \quad (7)$$

2) *Received communication signal*: At the DL preamble information period, pilot preambles are used to obtain channel state information (CSI) estimation [19]. At the DL data information period, the u -th UE receives the DL communication signal, and undergoes down-conversion, analog-to-digital conversion (ADC), CP removal, discrete Fourier transform (DFT), and other operations to get a received data \mathbf{Y}_u^C , which is expressed as

$$\mathbf{Y}_u^C = \sum_{b=1}^B \mathbf{X}_C^b \mathbf{H}_C^b + \mathbf{W}_u^C, \quad (8)$$

where $\mathbf{H}_C^b = [(\tilde{\mathbf{H}}_{u,m}^0)^T, \dots, (\tilde{\mathbf{H}}_{u,m}^{N_b-1})^T] \in \mathbb{C}^{N_b N_T \times N_U}$ with $\tilde{\mathbf{H}}_{u,m}^n = \sum_{l=0}^{L-1} \tilde{\mathbf{H}}_u^{l,b} e^{-j2\pi n l} \in \mathbb{C}^{N_T \times N_U}$, while $\tilde{\mathbf{H}}_u^{l,b}$ is the estimated CSI matrix; $\mathbf{X}_C^b = \text{diag}((\mathbf{X}_0^b)^T, \dots, (\mathbf{X}_{N_b-1}^b)^T) \in \mathbb{C}^{N_b M_b \times N_b N_T}$ is the transmit data; $\mathbf{W}_u^C \sim \mathcal{CN}(0, \sigma_C^2)$ is additive Gaussian white noise (AWGN) of dual-CC communication channel.

In terms of communication performance in CA-enabled MIMO-OFDM ISAC system, the closed-form communication MI is derived in Section IV-A.

C. Sensing Model

In the sensing channel model, the differences in attenuations caused by high and low-frequency bands are considered. Then, the sensing channel model of the b -th CC and received sensing signal are derived.

1) *Sensing channel model*: We assume that the radial velocity of a potential target is v_0 and the range to BS is r_0 . Meanwhile, the angle of arrive (AoA) and the angle of departure (AoD) between the target and BS are identical and are denoted by $\theta_{R_x} = \theta_{T_x}$. The transmit and received steering vectors are expressed as (9) and (10), respectively.

$$\mathbf{a}_{R_x}(\theta_{R_x}) = \left[e^{j2\pi p \left(\frac{d_r}{\lambda^b}\right) \sin(\theta_{R_x})} \right]_{p=0,1,\dots,N_R-1}, \quad (9)$$

$$\mathbf{a}_{T_x}(\theta_{T_x}) = \left[e^{j2\pi k \left(\frac{d_t}{\lambda^b}\right) \sin(\theta_{T_x})} \right]_{k=0,1,\dots,N_T-1}, \quad (10)$$

where p denotes the index of the receive antenna in BS; $\lambda^b = c/f_C^b$ is the wavelength with c being the speed of light.

The sensing channel model on the n -th subcarrier during the m -th OFDM symbol time in the b -th CC is expressed as

$$\mathbf{H}_{m,n}^b = \kappa_S^b e^{j2\pi(f_s^b m T^b - n \Delta f^b \tau_0)} \mathbf{a}_{R_x}(\theta_{R_x}) \mathbf{a}_{T_x}^T(\theta_{T_x}), \quad (11)$$

where $\mathbf{H}_{m,n}^b \in \mathbb{C}^{N_R \times N_T}$ and $\kappa_S^b = \sqrt{\frac{(\lambda^b)^2}{(4\pi)^3 r_0^4}} \beta_S^b$ is the attenuation between the target and BS with $\beta_S^b \sim \mathcal{CN}(0, \sigma_\beta^2)$ being the target RCS [20]; $f_s^b = \frac{2f_C^b v_0}{c}$ and $\tau_0 = \frac{2r_0}{c}$ are the Doppler frequency shift and delay, respectively.

2) *Received sensing signal*: At the receiver (Rx) of BS, the mixed echo signals on high and low-frequency bands are separated through matched filtering. Therefore, the received

echo signal on the n -th subcarrier during the m -th OFDM symbol time is denoted by

$$\begin{aligned} \mathbf{y}_{m,n}^S &= \mathbf{y}_{m,n}^{S,1} + \mathbf{y}_{m,n}^{S,2} \\ &= \sum_{b=1}^B \mathbf{H}_{m,n}^b \mathbf{x}_{m,n}^b + \mathbf{z}_{m,n}^S, \end{aligned} \quad (12)$$

where $\mathbf{y}_{m,n}^S \in \mathbb{C}^{N_R \times 1}$ and $\mathbf{y}_{m,n}^{S,b}$ denotes the echo signal in b -th CC; $\mathbf{x}_{m,n}^b \in \mathbb{C}^{N_T \times 1} = \mathbf{X}_n^b \Upsilon_m$ is the transmit data with $\Upsilon_m = [0, 0_1, \dots, 1_m, \dots, 0_{M_b-1}]^T \in \mathbb{C}^{M_b \times 1}$; $\mathbf{z}_{m,n}^S \sim \mathcal{CN}(0, \sigma_S^2) \in \mathbb{C}^{N_R \times 1}$ is an AWGN vector.

III. A NOVEL CA-ENABLED MIMO-OFDM ISAC SIGNAL PROCESSING METHOD

In this section, a novel CA-enabled MIMO-OFDM ISAC signal processing method is proposed, as shown in Fig. 2. Without loss of generality, we assume that the 1-st CC is on the low-frequency band and the 2-nd CC is on the high-frequency band. Through matched filtering at the Rx, the mixed echo signals on the two CCs are separated.

There are two challenges in sensing signal processing in the proposed ISAC system: 1) The initial phase misalignment of the echo signals on high and low-frequency bands due to attenuation and RCS; 2) The fusion of the sensing data on high and low-frequency bands with different physical-layer parameters, such as subcarrier spacing and symbol duration. Therefore, we consider both data-level and symbol-level fusion methods of the sensing data on high and low-frequency bands.

The data-level fusion method is as follows: After the separation of mixed echo signals on high and low-frequency bands, the joint angle-range-velocity estimation method proposed in [21] is applied to the echo signal on high-frequency band to yield the estimated range r_{data}^1 and velocity v_{data}^1 of target. Similarly, the estimated range r_{data}^2 and velocity v_{data}^2 of target are obtained by processing the echo signal on low-frequency band. Finally, the final estimation of range is $\hat{r}_{\text{data}} = (r_{\text{data}}^1 + r_{\text{data}}^2)/2$, while the final estimation of velocity is $\hat{v}_{\text{data}} = (v_{\text{data}}^1 + v_{\text{data}}^2)/2$. However, the sensing accuracy of data-level fusion method is low. Therefore, this paper proposes a two-stage symbol-level fusion method, including signal preprocessing stage and sensing information fusion stage, detailed in Section III-A.

A. Signal Preprocessing Stage

Facing the above challenges, one of the purposes of sensing preprocessing is to align the initial phases of the echo signals on high and low-frequency bands.

1) *Angle estimation*: With identical AoA and AoD for two CCs and high signal-to-noise ratio (SNR) of the echo signal on low-frequency band, we utilize the echo signal on low-frequency band to estimate AoA and AoD.

Firstly, we remove the transmit data $\mathbf{x}_{m,n}^1$ in $\mathbf{y}_{m,n}^{S,1}$ using known communication data, and the echo signal on low-frequency band by all antennas is

$$\begin{aligned} \hat{\mathbf{H}}_{m,n}^1 &= \mathbf{y}_{m,n}^{S,1} (\mathbf{x}_{m,n}^1)^H (\mathbf{x}_{m,n}^1 (\mathbf{x}_{m,n}^1)^H)^{-1} \\ &= \kappa_S^b e^{j2\pi(f_s^b m T^b - n \Delta f^b \tau_0)} \mathbf{a}_{R_x}(\theta_{R_x}) \mathbf{a}_{T_x}^T(\theta_{T_x}) \mathbf{I} + \mathbf{z}_{m,n}^{S,1}, \end{aligned} \quad (13)$$

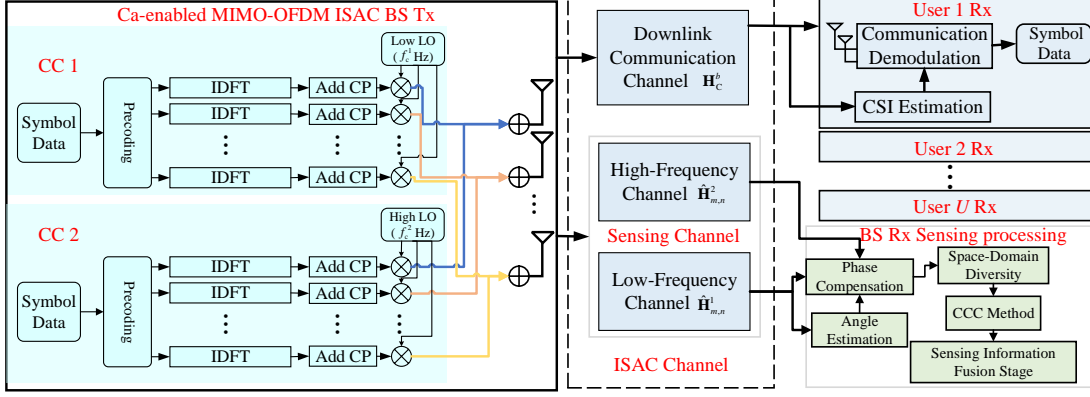


Fig. 2: CA-enabled MIMO-OFDM ISAC signal processing.

where $\hat{\mathbf{H}}_{m,n}^1 \in \mathbb{C}^{N_R \times N_T}$ and $\mathbf{I} \in \mathbb{C}^{N_T \times N_T}$ is the identity matrix; $\mathbf{z}_{m,n}^{S,1}$ is an AWGN matrix.

Upon observing $\hat{\mathbf{H}}_{m,n}^1$, it is obvious that the AoA introduces a linear phase shift along the received antenna elements. The AoA estimation is obtained using the conventional multiple signal classification (MUSIC) method [22], with the following steps.

Step 1: Calculate the covariance matrix $\mathbf{R}_{\hat{\mathbf{H}}_{m,n}^1}$ of signal $\hat{\mathbf{H}}_{m,n}^1$.

$$\mathbf{R}_{\hat{\mathbf{H}}_{m,n}^1} = \hat{\mathbf{H}}_{m,n}^1 \left[\hat{\mathbf{H}}_{m,n}^1 \right]^H. \quad (14)$$

Step 2: $\mathbf{R}_{\hat{\mathbf{H}}_{m,n}^1}$ is performed an eigenvalue decomposition (EVD) to obtain

$$\text{eig} \left(\mathbf{R}_{\hat{\mathbf{H}}_{m,n}^1} \right) = \mathbf{U}_s \mathbf{\Lambda}_s \mathbf{U}_s^H + \mathbf{U}_n \mathbf{\Lambda}_n \mathbf{U}_n^H, \quad (15)$$

where $\mathbf{\Lambda}_s$ and $\mathbf{\Lambda}_n$ denote the diagonal matrix of signal and noise, respectively; \mathbf{U}_s and \mathbf{U}_n represent the subspaces of signal and noise, respectively. The [22] proves that the noise subspace is orthogonal to the signal subspace. Therefore, we traverse the signal subspace to obtain AoA estimation.

Step 3: Generate a MUSIC spatial spectral vector

$$f_{\text{music}}(\theta) = \frac{1}{\mathbf{a}(\theta)^H \mathbf{U}_n \mathbf{U}_n^H \mathbf{a}(\theta)}, \quad (16)$$

where $\theta \in (0, \pi]$ and

$$\mathbf{a}(\theta) = \left[e^{j2\pi p \left(\frac{d_T}{\lambda_T} \right) \sin(\theta)} \right]_{p=0,1,\dots,N_R-1}^T. \quad (17)$$

Step 4: Search the peak of f_{music} to obtain the AoA estimation $\hat{\theta}_{\text{Rx}}$.

With the MUSIC method, the estimation result $\hat{\theta}_{\text{Rx}}$ of AoA is acquired for phase compensation.

2) *Phase compensation:* Phase compensation is designed to cancel known communication data, AoA, and AoD information contained in the echo signals on high and low-frequency bands. The echo signal by all antennas on the n -th subcarrier during the m -th OFDM symbol time in the b -th CC is expressed as

$$\mathbf{y}_{m,n}^{S,b} = \kappa_S^b e^{j2\pi(f_s^b m T^b - n \Delta f^b \tau_0)} \mathbf{a}_{\text{Rx}}(\theta_{\text{Rx}}) \mathcal{X}_{m,n}^b + \mathbf{z}_{m,n}^{S,b}, \quad (18)$$

where $\mathbf{y}_{m,n}^{S,b} \in \mathbb{C}^{N_R \times 1}$ and $\mathcal{X}_{m,n}^b = \mathbf{a}_{\text{Tx}}^T(\theta_{\text{Tx}}) \mathbf{x}_{m,n}^b \in \mathbb{C}$ is a transmit factor.

With the known transmit data and AoD estimation, we can compensate for $\mathcal{X}_{m,n}^b$ by multiplying the compensation factor $\tilde{\mathcal{X}}_{m,n}^b = \left(\mathbf{a}_{\text{Tx}}^T(\hat{\theta}_{\text{Tx}}) \mathbf{x}_{m,n}^b \right)^*$ on both sides of (18), denoted by

$$\mathbf{y}_{m,n}^{S,b} \tilde{\mathcal{X}}_{m,n}^b = \hat{\kappa}_S^b \kappa_S^b e^{j2\pi(f_s^b m T^b - n \Delta f^b \tau_0)} \mathbf{a}_{\text{Rx}}(\theta_{\text{Rx}}) + \mathbf{z}_{m,n}^{S,b} \tilde{\mathcal{X}}_{m,n}^b, \quad (19)$$

where $\hat{\mathcal{X}}_{m,n}^b = \mathcal{X}_{m,n}^b \tilde{\mathcal{X}}_{m,n}^b \in \mathbb{R}$. Then, with the AoA estimation, $\mathbf{a}_{\text{Rx}}(\theta_{\text{Rx}})$ in (19) is compensated, and $\mathbf{r}_{m,n}^{S,b}$ is expressed as

$$\mathbf{r}_{m,n}^{S,b} = \mathbf{h}_{m,n}^{S,b} + \mathbf{n}_{m,n}^{S,b}, \quad (20)$$

where

$$\mathbf{r}_{m,n}^{S,b} \in \mathbb{C}^{N_R \times 1} = \mathbf{y}_{m,n}^{S,b} \tilde{\mathcal{X}}_{m,n}^b \circ \mathbf{a}_{\text{Rx}}^*(\theta_{\text{Rx}}), \quad (21)$$

$$\mathbf{n}_{m,n}^{S,b} = \mathbf{z}_{m,n}^{S,b} \tilde{\mathcal{X}}_{m,n}^b \circ \mathbf{a}_{\text{Rx}}^*(\theta_{\text{Rx}}), \quad (22)$$

$$\mathbf{h}_{m,n}^{S,b} = \hat{\kappa}_S^b \kappa_S^b e^{j2\pi(f_s^b m T^b - n \Delta f^b \tau_0)} \mathbf{a}_{\text{Rx}}(\theta_{\text{Rx}}) \circ \mathbf{a}_{\text{Rx}}^*(\theta_{\text{Rx}}). \quad (23)$$

3) *Space-domain diversity:* Upon observing Eq. (23), the echo signals on each antenna are identical and can be coherently accumulated to improve SNR. The echo signal after coherent accumulation on the n -th subcarrier during the m -th OFDM symbol time in the b -th CC is expressed as

$$\mathbf{d}_{m,n}^{S,b} = \frac{1}{N_R} \sum_{p=0}^{N_R-1} \mathbf{r}_{m,n}^{S,b}(p), \quad (24)$$

where $\mathbf{r}_{m,n}^{S,b}(p)$ is the p -th element of $\mathbf{r}_{m,n}^{S,b}$. According to (24), the echo signal on N_b subcarriers during M_b OFDM symbol times in the b -th CC is written in matrix form as

$$\mathbf{D}^{S,b} = \mathbf{S}^{S,b} + \mathbf{Z}^{S,b}, \quad (25)$$

where $\mathbf{Z}^{S,b}$ is an AWGN matrix and $\mathbf{S}^{S,b} \in \mathbb{C}^{N_b \times M_b}$ denotes a delay-Doppler information matrix, expressed in (26).

4) *CCC method:* Observing (26), the initial phases of $\mathbf{S}^{S,b}$ on high and low-frequency bands are not aligned and there exists a different complex number $\hat{\kappa}_{m,n}^b \kappa_S^b$. To this end, a CCC method [23] is performed to eliminate the complex number $\hat{\kappa}_{m,n}^b \kappa_S^b$. Considering the noise, the procedure for applying the CCC method to $\mathbf{D}^{S,b}$ is presented in the following steps.

$$\mathbf{S}^{S,b} = \hat{\mathcal{X}}_{m,n}^b K_S^b \begin{bmatrix} 1 & e^{j2\pi f_s^b T^b} & \dots & e^{j2\pi(M_b-1)f_s^b T^b} \\ e^{-j2\pi\Delta f^b \tau_0} & e^{-j2\pi\Delta f^b \tau_0} e^{j2\pi f_s^b T^b} & \dots & e^{-j2\pi\Delta f^b \tau_0} e^{j2\pi(M_b-1)f_s^b T^b} \\ \vdots & \vdots & \ddots & \vdots \\ e^{-j2\pi(N_b-1)\Delta f^b \tau_0} & e^{-j2\pi(N_b-1)\Delta f^b \tau_0} e^{j2\pi f_s^b T^b} & \dots & e^{-j2\pi(N_b-1)\Delta f^b \tau_0} e^{j2\pi(M_b-1)f_s^b T^b} \end{bmatrix}. \quad (26)$$

$$\mathbf{R}_S^b = \frac{1}{M_b} \left[\frac{1}{N_b} \sum_{a=0}^{N_b-1} \mathbf{D}_a^{S,b} (\mathbf{D}_a^{S,b})^H, \frac{1}{N_b-1} \sum_{a=0}^{N_b-1} \mathbf{D}_{a+1}^{S,b} (\mathbf{D}_a^{S,b})^H, \dots, \frac{1}{N_b-n} \sum_{a=0}^{N_b-n-1} \mathbf{D}_{a+n}^{S,b} (\mathbf{D}_a^{S,b})^H, \dots, \mathbf{D}_{N_b-1}^{S,b} (\mathbf{D}_0^{S,b})^H \right]^T \quad (28)$$

$$= \left[1, e^{-j2\pi\Delta f^b \tau_0}, \dots, e^{-j2\pi n \Delta f^b \tau_0}, \dots, e^{-j2\pi(N_b-1)\Delta f^b \tau_0} \right]^T + \mathbf{z}^b.$$

$$\mathbf{V}_S^b = \frac{1}{N_b} \left[\frac{1}{M_b} \sum_{a=0}^{M_b-1} (\mathbf{C}_a^{S,b})^H \mathbf{C}_a^{S,b}, \frac{1}{M_b-1} \sum_{a=0}^{M_b-1} (\mathbf{C}_a^{S,b})^H \mathbf{C}_{a+1}^{S,b}, \dots, \frac{1}{M_b-n} \sum_{a=0}^{M_b-n-1} (\mathbf{C}_a^{S,b})^H \mathbf{C}_{a+n}^{S,b}, \dots, (\mathbf{C}_0^{S,b})^H \mathbf{C}_{N_b-1}^{S,b} \right] \quad (30)$$

$$= \left[1, e^{j2\pi \left(\frac{2f_C^b v_0}{c} \right) T^b}, \dots, e^{j2\pi m \left(\frac{2f_C^b v_0}{c} \right) T^b}, \dots, e^{j2\pi(M_b-1) \left(\frac{2f_C^b v_0}{c} \right) T^b} \right]^T + \mathbf{z}^b.$$

Step 1: $\mathbf{D}^{S,b}$ is divided into N_b row vectors, denoted by

$$\mathbf{D}^{S,b} = \left[(\mathbf{D}_0^{S,b})^T, (\mathbf{D}_1^{S,b})^T, \dots, (\mathbf{D}_{N_b-1}^{S,b})^T \right]^T, \quad (27)$$

where $\mathbf{D}_n^{S,b} \in \mathbb{C}^{1 \times M_b}$ represents the n -th row vector of $\mathbf{D}^{S,b}$.

Step 2: A delay feature vector $\mathbf{R}_S^b \in \mathbb{C}^{N_b \times 1}$ is obtained by accumulating the results of conjugate multiplication between the row vectors, denoted by (28), where \mathbf{z}^b is an AWGN vector.

Step 3: $\mathbf{D}^{S,b}$ is divided into M_b column vectors, expressed as

$$\mathbf{D}^{S,b} = \left[\mathbf{C}_0^{S,b}, \mathbf{C}_1^{S,b}, \dots, \mathbf{C}_{M_b-1}^{S,b} \right], \quad (29)$$

where $\mathbf{C}_m^{S,b} \in \mathbb{C}^{N_b \times 1}$ denotes the m -th column vector of $\mathbf{D}^{S,b}$.

Step 4: A Doppler feature vector $\mathbf{V}_S^b \in \mathbb{C}^{1 \times M_b}$ is obtained by accumulating the result of conjugate multiplication between the column vectors, expressed as (30). After the above steps, the four feature vectors are obtained, namely \mathbf{R}_S^1 , \mathbf{V}_S^1 , \mathbf{R}_S^2 , and \mathbf{V}_S^2 .

B. Sensing Information Fusion Stage

In the sensing information fusion stage, we fuse the feature vectors obtained in the signal preprocessing stage by the symbol-level fusion and estimate the parameters of target, which include the fusion algorithm of delay feature vectors and the fusion algorithm of Doppler feature vectors. Without loss of generality, the following remarks need to be specified.

- The subcarrier spacing is greater than ten times the Doppler frequency shift to ensure the orthogonality of OFDM signal [24]. The Doppler frequency shift is related to the carrier frequency, so that the subcarrier spacing is proportional to the carrier frequency and we assume that $\frac{\Delta f^2}{\Delta f^1} = \left\lfloor \frac{f_C^2}{f_C^1} \right\rfloor = Q$ ($Q > 1$), where $\lfloor \cdot \rfloor$ is floor function.
- Upon observing Fig. 2, the two CCs use discrete Add CP modules, allowing for the adjustment of CP lengths. It is

imperative to ensure that the maximum delay does not surpass the length of the shortest CP [7], [24].

1) Fusion algorithm of delay feature vectors: Without considering the noise, observing (28), the difference between \mathbf{R}_S^1 and \mathbf{R}_S^2 is the subcarrier spacing, which makes the symbol-level fusion difficult. According to $\frac{\Delta f^2}{\Delta f^1} = Q$, \mathbf{R}_S^1 and \mathbf{R}_S^2 are rewritten as

$$\mathbf{R}_S^1 = \left[e^{-j2\pi n \Delta f^1 \tau_0} \right]_{n=0,1,\dots,N_1-1}^T, \quad (31)$$

$$\mathbf{R}_S^2 = \left[e^{-j2\pi n Q \Delta f^1 \tau_0} \right]_{n=0,1,\dots,N_2-1}^T. \quad (32)$$

(32) is further rewritten as

$$\hat{\mathbf{R}}_S^2 = \left[e^{-j2\pi n'' \Delta f^1 \tau_0} \right]_{n''=0,Q,\dots,Q(N_2-1)}^T \in \mathbb{C}^{N_2 \times 1}. \quad (33)$$

Then, the subcarrier spacings in (31) and (33) are identical. The fusion process of delay feature vectors is discussed below in two cases.

Case 1 ($N_1 - 1 < Q(N_2 - 1)$): Initialize a zero-element vector $\mathbf{P}_S^1 \in \mathbb{C}^{Q N_2 \times 1}$ and an index value $\xi_1 \in \{0, 1, \dots, Q N_2 - 1\}$. Then, we traverse the element of \mathbf{P}_S^1 with ξ_1 . When ξ_1 equals n , the element $\mathbf{R}_S^1(n)$ is assigned to $\mathbf{P}_S^1(\xi_1)$. When ξ_1 equals n'' , the element $\hat{\mathbf{R}}_S^2(n'')$ is assigned to $\mathbf{P}_S^1(\xi_1)$. Given that the zero elements in \mathbf{P}_S^1 deteriorate the Fourier sidelobes, which can be mitigated by recovering the missing sensing data with the CS-based sensing method proposed in [11]. The final processed vector is denoted by $\hat{\mathbf{P}}_S^1$.

Case 2 ($N_1 - 1 \geq Q(N_2 - 1)$): Initialize a zero-element vector $\mathbf{P}_S^2 \in \mathbb{C}^{N_1 \times 1}$ and an index value $\xi_2 \in \{0, 1, \dots, N_1 - 1\}$. Then, we traverse the element of \mathbf{P}_S^2 with ξ_2 . When ξ_2 equals n , the element $\mathbf{R}_S^1(n)$ is assigned to $\mathbf{P}_S^2(\xi_2)$. When ξ_2 equals n'' , the element $\hat{\mathbf{R}}_S^2(n'')$ is assigned to $\mathbf{P}_S^2(\xi_2)$.

Taking the $\hat{\mathbf{P}}_S^1$ in **Case 1** as an example, an improved IDFT method is used to achieve a high-accuracy sensing. The specific procedures are as follows, while the **Case 2** has the

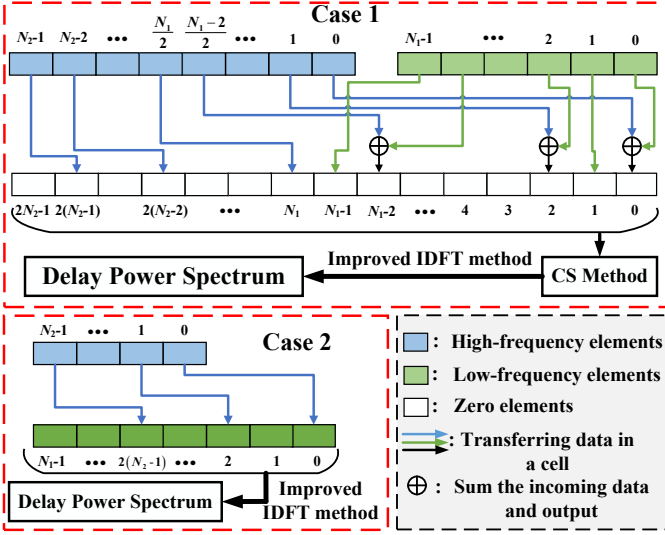


Fig. 3: Fusion algorithm of delay feature vectors when $Q = 2$.

similar procedures.

Step 1: Obtain a searching interval $[R_{\min}, R_{\max}]$ based on the sensing demands in the application scenario of ISAC [25].

Step 2: Generate a distance searching vector $\vec{\mathbf{A}}$ by gridding the searching interval with a size of grid being $\Delta R = \frac{R_{\max} - R_{\min}}{J}$, where J is the number of grids and $\vec{\mathbf{A}} \in \mathbb{C}^{J \times 1}$ is denoted by

$$\vec{\mathbf{A}} = [R_1, R_2, \dots, R_\eta, \dots, R_J]^T, \quad (34)$$

with $\eta \in \{1, 2, \dots, J\}$ denoting the index of grids.

Step 3: According to the size of $\hat{\mathbf{P}}_S^1$ and the expression form of delay feature vectors in (31), the $\vec{\mathbf{A}}$ is transformed to a searching matrix $\mathbf{A}_1 \in \mathbb{C}^{J \times QN_2}$, which is expressed as

$$\mathbf{A}_1 = \begin{bmatrix} 1 & e^{j2\pi\Delta f^1 \frac{2R_1}{c}} & \dots & e^{j2\pi(QN_2-1)\Delta f^1 \frac{2R_1}{c}} \\ 1 & e^{j2\pi\Delta f^1 \frac{2R_2}{c}} & \dots & e^{j2\pi(QN_2-1)\Delta f^1 \frac{2R_2}{c}} \\ \vdots & \vdots & \ddots & \vdots \\ 1 & e^{j2\pi\Delta f^1 \frac{2R_J}{c}} & \dots & e^{j2\pi(QN_2-1)\Delta f^1 \frac{2R_J}{c}} \end{bmatrix}. \quad (35)$$

Step 4: Obtain and search the delay profile $\vec{\mathbf{P}}_1 = \mathbf{A}_1 \hat{\mathbf{P}}_S^1$. The peak index of $\vec{\mathbf{P}}_1$ is denoted by $\hat{\eta}_1$.

Step 5: The range estimation of target is $\hat{r}_0^1 = \vec{\mathbf{A}}(\hat{\eta}_1)$.

The fusion algorithm of delay feature vectors is shown in **Algorithm 1**, which is explained intuitively in Fig. 3.

2) *Fusion algorithm of Doppler feature vectors:* Without considering the noise, observing (30), the different parameters between \mathbf{V}_S^1 and \mathbf{V}_S^2 are carrier frequency and total symbol duration. (30) is rewritten as

$$\mathbf{V}_S^b = \left[e^{j2\pi m \frac{2v_0}{c}} (f_C^b T^b) \right]_{|m=0,1,\dots,M_b-1}, \quad (36)$$

where $f_C^b T^b = f_C^b \left(\frac{1}{\Delta f^b} + T_s^b \right)$. If $f_C^1 T^1 = f_C^2 T^2$, \mathbf{V}_S^1 and \mathbf{V}_S^2 can be coherently accumulated to obtain a SNR gain.

Fortunately, as shown in Section III-B, the unique framework of the proposed CA-enabled MIMO-OFDM ISAC system supports adjustable durations of CPs in the two CCs. Meanwhile, **Theorem 1** proves that $f_C^1 T^1 = f_C^2 T^2$.

Algorithm 1: Fusion algorithm of Delay feature vectors

Input: Delay feature vectors \mathbf{R}_S^1 and \mathbf{R}_S^2 ;
The number of subcarriers N_1 and N_2 ;
The subcarriers spacing Δf^1 and Δf^2 .

Output: The range estimations of target \hat{r}_0^1 and \hat{r}_0^2 .

- 1: **if** $N_1 - 1 \geq Q(N_2 - 1)$ **do**
- 2: Assume a vector $\mathbf{P}_S^2 \in \mathbb{C}^{N_1 \times 1} = \mathbf{R}_S^1$,
and an index value $\mu_2 \in \mathcal{N}_2 = \{0, 1, \dots, N_2 - 1\}$;
- 3: **for** \mathbf{P}_S^2 μ_2 in \mathcal{N}_2 **do**
- 4: The element value of $\mathbf{R}_S^2(\mu_2)$ is added to $\mathbf{P}_S^2(Q\mu_2)$;
- 5: $\mathbf{P}_S^2(Q\mu_2) = \mathbf{P}_S^2(Q\mu_2)/2$;
- 6: **end for**
- 7: **else if** $N_1 - 1 < Q(N_2 - 1)$ **do**
- 8: Initialize a zero-element vector $\mathbf{P}_S^1 \in \mathbb{C}^{QN_2 \times 1}$,
and an index value $\mu_1 \in \mathcal{N}_1 = \{0, 1, \dots, N_1 - 1\}$;
- 9: **for** \mathbf{P}_S^1 μ_1 in \mathcal{N}_1 **do**
- 10: The element value of $\mathbf{R}_S^1(\mu_1)$ is assigned to $\mathbf{P}_S^1(\mu_1)$;
- 11: **end for**
- 12: Initialize an index value $\mu_3 \in \mathcal{N}_3 = \{0, 1, \dots, N_2 - 1\}$;
- 13: **for** \mathbf{P}_S^1 μ_3 in \mathcal{N}_3 **do**
- 14: The element value of $\mathbf{R}_S^2(\mu_3)$ is added to $\mathbf{P}_S^1(Q\mu_3)$;
- 15: **if** $Q\mu_3 \leq N_1 - 1$ **do**
- 16: $\mathbf{P}_S^1(Q\mu_3) = \mathbf{P}_S^1(Q\mu_3)/2$;
- 17: **end if**
- 18: **end for**
- 19: Recover the missing elements of \mathbf{P}_S^1 by
CS-based method proposed in [11] to obtain $\hat{\mathbf{P}}_S^1$;
- 20: **end if**
- 21: The results of $\hat{\mathbf{P}}_S^1$ and \mathbf{P}_S^2 undergoing improved IDFT are
searched for peaks to obtain the peak indices $\hat{\eta}^1$ and $\hat{\eta}^2$;
- 22: Substitute $\hat{\eta}^1$ and $\hat{\eta}^2$ into (34) to obtain the range
estimations of target \hat{r}_0^1 and \hat{r}_0^2 .

Theorem 1: According to $\left\lfloor \frac{f_C^2}{f_C^1} \right\rfloor = Q$, we assume that $\frac{f_C^2}{f_C^1} = Q + \rho$ ($\rho < 1$). $f_C^1 T^1 = f_C^2 T^2$ can be satisfied when

$$N_s^1 = \left(1 + \frac{\rho}{Q} \right) \frac{N_1}{N_2} N_s^2 + \frac{N_1 \rho}{Q}. \quad (37)$$

Proof. Based on $\frac{f_C^2}{f_C^1} = \frac{\Delta f^2}{\Delta f^1} + \rho$, the relationship between T_s^1 and T_s^2 is expressed as

$$\begin{aligned} f_C^1 \left(\frac{1}{\Delta f^1} + T_s^1 \right) &= f_C^2 \left(\frac{1}{\Delta f^2} + T_s^2 \right), \\ \Rightarrow \left(\frac{f_C^1}{\Delta f^1} + f_C^1 T_s^1 \right) &= f_C^1 \left(\frac{\Delta f^2}{\Delta f^1} + \rho \right) \left(\frac{1}{\Delta f^2} + T_s^2 \right), \\ \Rightarrow T_s^1 &= (Q + \rho) T_s^2 + \frac{\rho}{\Delta f^2}. \end{aligned} \quad (38)$$

Then, according to $T_s^b = \frac{N_s^b T_{\text{ofdm}}^b}{N_b}$, the relationship between N_s^1 and N_s^2 can be expressed as

$$\begin{aligned} \frac{N_s^1 T_{\text{ofdm}}^1}{N_1} &= (Q + \rho) \frac{N_s^2 T_{\text{ofdm}}^2}{N_2} + \frac{\rho}{\Delta f^2}, \\ \Rightarrow N_s^1 &= \left(\frac{Q + \rho}{Q} \right) \frac{N_1}{N_2} N_s^2 + \frac{N_1 \rho}{Q}. \end{aligned} \quad (39)$$

The fusion process of Doppler feature vectors is revealed in the following three cases.

Case 1 ($M_1 > M_2$): Initialize a zero-element vector $\mathbf{E}_S^1 \in \mathbb{C}^{1 \times M_1}$ and complement \mathbf{V}_S^2 with zero to get the matrix $\hat{\mathbf{V}}_S^2 \in \mathbb{C}^{1 \times M_1} = [\mathbf{V}_S^2, 0_{M_2}, \dots, 0_{M_1-1}]$. Then, the processed vector $\mathbf{E}_S^1 = (\mathbf{V}_S^1 + \hat{\mathbf{V}}_S^2)/2$ is obtained.

Case 2 ($M_1 < M_2$): Initialize a zero-element vector $\mathbf{E}_S^2 \in \mathbb{C}^{1 \times M_2}$ and complement \mathbf{V}_S^1 with zero to get the matrix $\hat{\mathbf{V}}_S^1 \in \mathbb{C}^{1 \times M_2} = [\mathbf{V}_S^1, 0_{M_1}, \dots, 0_{M_2-1}]$. Then, the processed vector

$\mathbf{E}_S^2 = (\hat{\mathbf{V}}_S^1 + \mathbf{V}_S^2)/2$ is obtained.

Case 3 ($M_1 = M_2 = M$): Initialize a zero-element vector $\mathbf{E}_S^3 \in \mathbb{C}^{1 \times M}$ and obtain a vector $\mathbf{E}_S^3 = (\mathbf{V}_S^1 + \mathbf{V}_S^2)/2$.

Taking the \mathbf{E}_S^1 in **Case 1** as an example, an improved discrete Fourier transform (DFT) method is applied to achieve high-accuracy sensing. The specific procedures are as follows, while the **Case 2** and **Case 3** have the similar procedures.

Step 1: Obtain a searching interval $[V_{\min}, V_{\max}]$ based on the sensing demands in the application scenario of ISAC [25].

Step 2: Generate a velocity searching vector $\vec{\mathbf{B}}$ by gridding the searching interval with a size of grid being $\Delta V = \frac{V_{\max} - V_{\min}}{G}$, where G is the number of grids and $\vec{\mathbf{B}} \in \mathbb{C}^{1 \times G}$ is expressed as

$$\vec{\mathbf{B}} = [V_1, V_2, \dots, V_g, \dots, V_G], \quad (40)$$

with $g \in \{1, 2, \dots, G\}$ representing the index of grids.

Step 3: According to the size of \mathbf{E}_S^1 and the expression form of Doppler feature vectors in (30), $\vec{\mathbf{B}}$ is transformed to a searching matrix $\mathbf{B}_1 \in \mathbb{C}^{M_1 \times G}$, which is expressed as

$$\mathbf{B}_1 = \begin{bmatrix} 1 & e^{-j2\pi f_C^1 T^1 \frac{2V_1}{c}} & \dots & e^{-j2\pi(M_1-1)f_C^1 T^1 \frac{2V_1}{c}} \\ 1 & e^{-j2\pi f_C^1 T^1 \frac{2V_2}{c}} & \dots & e^{-j2\pi(M_1-1)f_C^1 T^1 \frac{2V_2}{c}} \\ \vdots & \vdots & \ddots & \vdots \\ 1 & e^{-j2\pi f_C^1 T^1 \frac{2V_G}{c}} & \dots & e^{-j2\pi(M_1-1)f_C^1 T^1 \frac{2V_G}{c}} \end{bmatrix}^T. \quad (41)$$

Step 4: Obtain and search the Doppler profile $\vec{\mathbf{E}}_1 = \mathbf{E}_S^1 \mathbf{B}_1$. The peak index of $\vec{\mathbf{E}}_1$ is denoted by \hat{g}_1 .

Step 5: The velocity estimation of target is $\hat{v}_0^1 = \vec{\mathbf{B}}(\hat{g}_1)$.

The fusion algorithm of Doppler feature vectors is shown in **Algorithm 2**, which is explained intuitively in Fig. 4.

Algorithm 2 : Fusion algorithm of Doppler feature vectors

Input: Doppler feature vectors \mathbf{V}_S^1 and \mathbf{V}_S^2 ;
The number of OFDM symbols M_1 and M_2 ;
The carrier frequencies f_C^1 and f_C^2 ;
The total OFDM duration T^1 and T^2 .

Output: The velocity estimations of target \hat{v}_0^1 , \hat{v}_0^2 , and \hat{v}_0^3 .

- 1: **if** $M_1 > M_2$ **do**
- 2: Assume a vector $\mathbf{E}_S^1 \in \mathbb{C}^{1 \times M_1} = \mathbf{V}_S^1$,
 and an index value $\omega_1 \in \mathcal{M}_1 = \{0, 1, \dots, M_2 - 1\}$;
- 3: **for** \mathbf{E}_S^2 ω_1 in \mathcal{M}_1 **do**
- 4: The element value of $\mathbf{V}_S^2(\omega_1)$ is added to $\mathbf{E}_S^1(\omega_1)$;
- 5: $\mathbf{E}_S^1(\omega_1) = \mathbf{E}_S^1(\omega_1)/2$;
- 6: **end for**
- 7: **else if** $M_1 < M_2$ **do**
- 8: Assume a vector $\mathbf{E}_S^2 \in \mathbb{C}^{1 \times M_2} = \mathbf{V}_S^2$,
 and an index value $\omega_2 \in \mathcal{M}_2 = \{0, 1, \dots, M_1 - 1\}$;
- 9: **for** \mathbf{E}_S^1 ω_2 in \mathcal{M}_2 **do**
- 10: The element value of $\mathbf{V}_S^1(\omega_2)$ is added to $\mathbf{E}_S^2(\omega_2)$;
- 11: $\mathbf{E}_S^2(\omega_2) = \mathbf{E}_S^2(\omega_2)/2$;
- 12: **end for**
- 13: **else if** $M_1 = M_2 = M$ **do**
- 14: Initialize a zero-elements vector $\mathbf{E}_S^3 \in \mathbb{C}^{1 \times M}$,
 and an index value $\omega_3 \in \mathcal{M}_3 = \{0, 1, \dots, M - 1\}$;
- 15: **for** \mathbf{E}_S^3 ω_3 in \mathcal{M}_3 **do**
- 16: $\mathbf{E}_S^3(\omega_3) = [\mathbf{V}_S^1(\omega_3) + \mathbf{V}_S^2(\omega_3)]/2$;
- 17: **end for**
- 18: **end if**
- 19: The results of \mathbf{E}_S^1 , \mathbf{E}_S^2 , and \mathbf{E}_S^3 undergoing improved DFT are searched for peaks to obtain the peak indices \hat{g}_1 , \hat{g}_2 , and \hat{g}_3 ;
- 20: Substitute \hat{g}_1 , \hat{g}_2 , and \hat{g}_3 into (40) to obtain the velocity estimations of target \hat{v}_0^1 , \hat{v}_0^2 , and \hat{v}_0^3 .

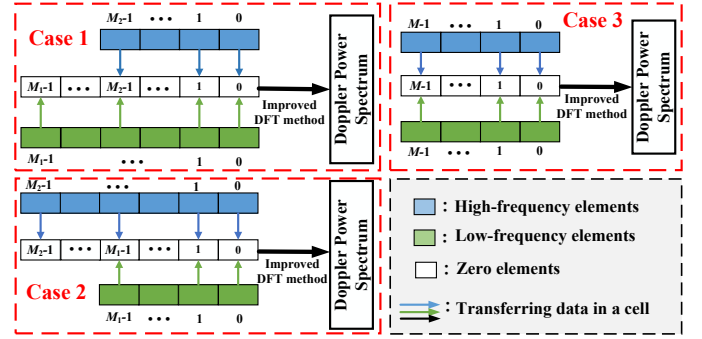


Fig. 4: Fusion algorithm of Doppler feature vectors.

IV. PERFORMANCE ANALYSIS

In this section, communication MI is used to characterize the channel capacity of the proposed ISAC system, and CRLB is used as a performance metric of sensing for the proposed ISAC system [26].

A. Communication Performance Analysis

In this section, the closed-form communication MI of the proposed CA-enabled MIMO-OFDM ISAC system is derived with the assumption of known communication CSI at both the BS and UE.

1) *Communication MI of MIMO-OFDM ISAC system:* The communication MI for MIMO-OFDM ISAC system is provided in **Lemma 1**.

Lemma 1: According to the signal model in (42), the communication MI of the MIMO-OFDM ISAC system is obtained in (43), with N_x , N_c , and N_r denoting the number of OFDM symbols, subcarriers, and received antennas, respectively [27].

$$\mathbf{Y}_{\text{com}} = \mathbf{X}\mathbf{H} + \mathbf{W}_{\text{com}}, \quad (42)$$

$$I(\mathbf{X}; \mathbf{Y}_{\text{com}} | \mathbf{H}) = N_x \log_2 \left[\left(\sigma_Z^2 \right)^{-N_r N_c} \det \left(\mathbf{H}^H \frac{E\{\mathbf{X}^H \mathbf{X}\}}{N_x} \mathbf{H} + \sigma_Z^2 \mathbf{I}_{N_r N_c} \right) \right], \quad (43)$$

where $\mathbf{W}_{\text{com}} \sim \mathcal{CN}(0, \sigma_Z^2)$.

2) *Communication MI of the proposed CA-enabled MIMO-OFDM ISAC system:* According to [27] and (8), the communication MI of the proposed CA-enabled MIMO-OFDM ISAC system is defined as

$$I(\mathbf{X}_C^1, \mathbf{X}_C^2; \mathbf{Y}_u^C | \mathbf{H}_C^1, \mathbf{H}_C^2). \quad (44)$$

Since the frequency bands between the two CCs are far separated and transmit data independently, \mathbf{X}_C^1 and \mathbf{X}_C^2 are independent, as well as \mathbf{H}_C^1 and \mathbf{H}_C^2 . Therefore, (44) is rewritten as

$$\begin{aligned} & I(\mathbf{X}_C^1, \mathbf{X}_C^2; \mathbf{Y}_u^C | \mathbf{H}_C^1, \mathbf{H}_C^2) \\ &= I(\mathbf{X}_C^1; \mathbf{Y}_u^C | \mathbf{H}_C^1, \mathbf{H}_C^2) + I(\mathbf{X}_C^2; \mathbf{Y}_u^C | \mathbf{X}_C^1, \mathbf{H}_C^1, \mathbf{H}_C^2) \\ &= h(\mathbf{Y}_u^C | \mathbf{H}_C^1, \mathbf{H}_C^2) - h(\mathbf{Y}_u^C | \mathbf{X}_C^1, \mathbf{H}_C^1, \mathbf{H}_C^2) \\ &\quad + h(\mathbf{Y}_u^C | \mathbf{X}_C^1, \mathbf{H}_C^1, \mathbf{H}_C^2) - h(\mathbf{Y}_u^C | \mathbf{X}_C^1, \mathbf{X}_C^2, \mathbf{H}_C^1, \mathbf{H}_C^2) \\ &= h(\mathbf{Y}_u^C | \mathbf{H}_C^1, \mathbf{H}_C^2) - h(\mathbf{W}_u^C). \end{aligned} \quad (45)$$

$$\begin{aligned}
p(\mathbf{Y}_u^C | \mathbf{H}_C^1, \mathbf{H}_C^2) &= \prod_{j=1}^{NM} p(\mathbf{y}_u^{C,j} | \mathbf{H}_C^1, \mathbf{H}_C^2) \\
&= \prod_{j=1}^{NM} \frac{1}{\pi^{N_U} \det \left[\sum_{b=1}^{\mathcal{B}} \left[(\mathbf{H}_C^b)^H E \left\{ (\mathbf{X}_C^{b,j})^H \mathbf{X}_C^{b,j} \right\} \mathbf{H}_C^b \right] + \sigma_C^2 \mathbf{I}_{N_U} \right]} \exp \left\{ - \left[\left(\sum_{b=1}^{\mathcal{B}} \left[(\mathbf{H}_C^b)^H E \left\{ (\mathbf{X}_C^{b,j})^H \mathbf{X}_C^{b,j} \right\} \mathbf{H}_C^b \right] + \sigma_C^2 \mathbf{I}_{N_U} \right)^{-1} \mathbf{y}_u^{C,j} (\mathbf{y}_u^{C,j})^H \right] \right\} \\
&= \prod_{j=1}^N \frac{1}{\pi^{MN_U} \det^M \left[\sum_{b=1}^{\mathcal{B}} \left[(\tilde{\mathbf{H}}_{u,m}^n)^H E \left\{ (\mathbf{X}_n^{b,j})^H \mathbf{X}_n^{b,j} \right\} \tilde{\mathbf{H}}_{u,m}^n \right] + \sigma_C^2 \mathbf{I}_{N_U} \right]} \\
&\quad \times \exp \left\{ -\text{tr} \left[\sum_{j=1}^M \left(\sum_{b=1}^{\mathcal{B}} \left[(\tilde{\mathbf{H}}_{u,m}^n)^H E \left\{ (\mathbf{X}_n^{b,j})^H \mathbf{X}_n^{b,j} \right\} \tilde{\mathbf{H}}_{u,m}^n \right] + \sigma_C^2 \mathbf{I}_{N_U} \right)^{-1} \mathbf{y}_u^{C,j} (\mathbf{y}_u^{C,j})^H \right] \right\}, \tag{47}
\end{aligned}$$

$$\begin{aligned}
h(\mathbf{Y}_u^C | \mathbf{H}_C^1, \mathbf{H}_C^2) &= \sum_{n=0}^{N-1} \left\{ MN_U \log_2 \pi + MN_U \log_2 e + M \log_2 \left[\det \left(\sum_{b=1}^{\mathcal{B}} \left[(\tilde{\mathbf{H}}_{u,m}^n)^H E \left\{ (\mathbf{X}_n^{b,j})^H \mathbf{X}_n^{b,j} \right\} \tilde{\mathbf{H}}_{u,m}^n \right] + \sigma_C^2 \mathbf{I}_{N_U} \right) \right] \right\}. \tag{48}
\end{aligned}$$

$$\begin{aligned}
I(\mathbf{X}_C^1, \mathbf{X}_C^2; \mathbf{Y}_u^C | \mathbf{H}_C^1, \mathbf{H}_C^2) &= M \sum_{n=0}^{N-1} \log_2 \left[(\sigma_C^2)^{-N_U} \det \left(\sum_{b=1}^{\mathcal{B}} \left[(\tilde{\mathbf{H}}_{u,m}^n)^H E \left\{ (\mathbf{X}_n^{b,j})^H \mathbf{X}_n^{b,j} \right\} \tilde{\mathbf{H}}_{u,m}^n \right] + \sigma_C^2 \mathbf{I}_{N_U} \right) \right] \\
&= M \log_2 \left[(\sigma_C^2)^{-N_U N} \prod_{n=0}^{N-1} \det \left(\sum_{b=1}^{\mathcal{B}} \left[(\tilde{\mathbf{H}}_{u,m}^n)^H E \left\{ (\mathbf{X}_n^{b,j})^H \mathbf{X}_n^{b,j} \right\} \tilde{\mathbf{H}}_{u,m}^n \right] + \sigma_C^2 \mathbf{I}_{N_U} \right) \right] \\
&= M \log_2 \left[(\sigma_C^2)^{-N_U N} \det \left(\sum_{b=1}^{\mathcal{B}} \left[(\mathbf{H}^b)^H \text{diag} \left\{ E \left\{ (\mathbf{X}_C^{b,j})^H \mathbf{X}_C^{b,j} \right\} \right\} \mathbf{H}^b \right] + \sigma_C^2 \mathbf{I}_{N_U N} \right) \right] \\
&= M \log_2 \left[(\sigma_C^2)^{-N_U N} \det \left[\sum_{b=1}^{\mathcal{B}} \left[(\mathbf{H}^b)^H E \left\{ \frac{(\mathbf{X}_C^b)^H \mathbf{X}_C^b}{M} \right\} \mathbf{H}^b \right] + \sigma_C^2 \mathbf{I}_{N_U N} \right] \right], \tag{50}
\end{aligned}$$

Theorem 2: According to (8) and (45), the communication MI of the proposed CA-enabled MIMO-OFDM ISAC system is expressed as

$$\begin{aligned}
I(\mathbf{x}_C^1, \mathbf{x}_C^2; \mathbf{y}_u^C | \mathbf{H}_C^1, \mathbf{H}_C^2) &= \\
M \log_2 \left[(\sigma_C^2)^{-N_U N} \det \left(\sum_{b=1}^{\mathcal{B}} \left[(\mathbf{H}^b)^H E \left[\frac{(\mathbf{x}_C^b)^H \mathbf{x}_C^b}{M} \right] \mathbf{H}^b \right] + \sigma_C^2 \mathbf{I}_{N_U N} \right) \right]. \tag{46}
\end{aligned}$$

Proof. For ease of derivation, we consider the assumptions of $N_1 = N_2 = N$ and $M_1 = M_2 = M$. Since \mathbf{X}_C^b is a block diagonal array, the probability density function (PDF) of \mathbf{Y}_u^C under known CSI is the product of the PDFs on the N subcarriers, denoted by (47), where $\mathbf{y}_u^{C,j}$ is the j -th row or column vector of \mathbf{Y}_u^C , and \mathbf{I}_{N_U} represents a $N_U \times N_U$ unit matrix. According to (47), the entropy matrix $h(\mathbf{Y}_u^C | \mathbf{H}_C^1, \mathbf{H}_C^2)$ is obtained as in (48). Meanwhile, the noise entropy $h(\mathbf{W}_u^C)$ can be obtained as

$$\begin{aligned}
h(\mathbf{W}_u^C) &= NMN_U \log_2 \pi + NMN_U \log_2 e \\
&\quad + NM \log_2 [\det(\sigma_C^2 \mathbf{I}_{N_U})]. \tag{49}
\end{aligned}$$

Therefore, substituting (48) and (49) into (45), the communication MI of the proposed CA-enabled MIMO-OFDM ISAC system in (46) is derived in (50), where the \mathbf{H}^b is the

transformation of \mathbf{H}_C^b in (8), expressed as follows

$$\mathbf{H}^b = \text{diag} \left\{ \tilde{\mathbf{H}}_{u,m}^0, \dots, \tilde{\mathbf{H}}_{u,m}^{N-1} \right\} \in \mathbb{C}^{N_T N \times N_U N}. \tag{51}$$

B. Sensing Performance Analysis

The CRLB is generally used to determine the lower bound on the variance of unbiased estimator and characterize the sensing ability of a signal [28]. Therefore, the CRLB of the CA-enabled MIMO-OFDM ISAC system is derived in this section.

1) *CRLB of MIMO-OFDM system:* The CRLB for OFDM ISAC system is derived in [7], and the CRLB for MIMO-OFDM ISAC system is revealed in **Theorem 3**. For ease of derivation, $\gamma = \frac{2v_0}{c}$ is used as an estimation of velocity to avoid the impact of different carrier frequency on theoretical derivation [7]. Meanwhile, $\sin \theta_{R_x}$ is used as an estimation of AoA to avoid the presence of unknown parameters after multiple derivations.

Theorem 3: For a MIMO-OFDM ISAC system (e.g., the b -th CC), the CRLBs of $\sin \theta_{R_x}$, τ_0 , and γ are expressed as

$$\Gamma_{\text{mimo}} = \frac{1}{\varpi \cdot (2\pi)^2} \frac{1}{M_b N_b N_U \Theta_b^p \Theta_b^n \Theta_b^m + 2\Theta_b^{p,n} \Theta_b^{p,m} \Theta_b^{m,n} - N_b (\Theta_b^{p,m})^2 \Theta_b^n - M_b (\Theta_b^{p,n})^2 \Theta_b^m - N_U (\Theta_b^{m,n})^2 \Theta_b^p}, \quad (55)$$

$$\Gamma_{\text{ca}} = \frac{1}{\varpi \cdot (2\pi)^2} \frac{1}{M N N_U \Theta_B^p \Theta_B^n \Theta_B^m + 2\Theta_B^{p,n} \Theta_B^{p,m} \Theta_B^{m,n} - N (\Theta_B^{p,m})^2 \Theta_B^n - M (\Theta_B^{p,n})^2 \Theta_B^m - N_U (\Theta_B^{m,n})^2 \Theta_B^p}, \quad (58)$$

(52), (53), and (54), respectively.

$$\text{CRLB}(\sin \theta_{\text{Rx}}) = \frac{\Gamma_{\text{mimo}} N_U [M_b N_b \Theta_b^n \Theta_b^m - (\Theta_b^{m,n})^2]}{M_b N_b}, \quad (52)$$

$$\text{CRLB}(\tau_0) = \frac{\Gamma_{\text{mimo}} N_b [M_b N_U \Theta_b^p \Theta_b^m - (\Theta_b^{p,m})^2]}{M_b N_U}, \quad (53)$$

$$\text{CRLB}(\gamma) = \frac{\Gamma_{\text{mimo}} M_b [N_b N_U \Theta_b^p \Theta_b^n - (\Theta_b^{p,n})^2]}{N_b N_U}, \quad (54)$$

where Γ_{mimo} is denoted by (55), $\varpi = \frac{|A|^2}{\sigma^2}$, $\Theta_b^n = \sum_n (n \Delta f^b)^2$, $\Theta_b^m = \sum_m (m f_C^b T^b)^2$, $\Theta_b^p = \sum_p (p \frac{d_r}{\lambda^b})^2$, $\Theta_b^{m,n} = \sum_m \sum_n mn \Delta f^b f_C^b T^b$, $\Theta_b^{p,n} = \sum_p \sum_n pn \frac{d_r}{\lambda^b} \Delta f^b$, and $\Theta_b^{p,m} = \sum_p \sum_m pm \frac{d_r}{\lambda^b} f_C^b T^b$.

Proof. Please refer to **Appendix A**. ■

2) *CRLB of CA-enabled MIMO-OFDM system:* The CRLBs of range and velocity estimations of the proposed ISAC system are derived. For simplicity, two CCs occupy the same number of resource elements (REs), i.e., $N_1 = N_2 = N$ and $M_1 = M_2 = M$.

According to (12), the CRLBs of τ_0 and γ for the proposed CA-enabled MIMO-OFDM ISAC system are expressed as (56) and (57), respectively.

$$\text{CRLB}_{\text{CA}}(\tau_0) = \frac{\Gamma_{\text{ca}} N [M N_U \Theta_B^p \Theta_B^m - (\Theta_B^{p,m})^2]}{M N_U}, \quad (56)$$

$$\text{CRLB}_{\text{CA}}(\gamma) = \frac{\Gamma_{\text{ca}} M [N N_U \Theta_B^p \Theta_B^n - (\Theta_B^{p,n})^2]}{N N_U}, \quad (57)$$

where Γ_{ca} is expressed in (58), $\Theta_B^n = \sum_n (n (\Delta f^1 + \Delta f^2))^2$, $\Theta_B^m = \sum_m (m (f_C^1 T^1 + f_C^2 T^2))^2$, $\Theta_B^p = \sum_p (p (\frac{d_r}{\lambda^1} + \frac{d_r}{\lambda^2}))^2$, and

$$\Theta_B^{m,n} = \sum_m \sum_n mn (\Delta f^1 + \Delta f^2) (f_C^1 T^1 + f_C^2 T^2),$$

$$\Theta_B^{p,n} = \sum_p \sum_n pn \left(\frac{d_r}{\lambda^1} + \frac{d_r}{\lambda^2} \right) (\Delta f^1 + \Delta f^2),$$

$$\Theta_B^{p,m} = \sum_p \sum_m pm \left(\frac{d_r}{\lambda^1} + \frac{d_r}{\lambda^2} \right) (f_C^1 T^1 + f_C^2 T^2).$$

Substituting $\Delta f^2 = Q \Delta f^1$ and $f_C^1 T^1 = f_C^2 T^2$ mentioned in Section III-B into (56) and (57), the simplest close-form

expressions for CRLBs of τ_0 and γ are

$$\text{CRLB}_{\text{CA}}(\tau_0) = \frac{\Gamma_{\text{CA}} \left[\frac{(2N_U)(2M-1)}{36} - \frac{(N_U-1)(M-1)}{16} \right]}{(\Delta f^1)^2 (Q+1)^2 (N-1)}, \quad (59)$$

$$\text{CRLB}_{\text{CA}}(\gamma) = \frac{\Gamma_{\text{CA}} \left[\frac{(2N_U)(2N-1)}{36} - \frac{(N_U-1)(N-1)}{16} \right]}{(2f_C^1 T^1)^2 (M-1)}, \quad (60)$$

where Γ_{CA} is expressed in (61).

According to $\tau_0 = \frac{2R}{c}$ and $\gamma = \frac{2v_0}{c}$, the CRLBs of R and v_0 of CA-enabled MIMO-OFDM ISAC system are

$$\text{CRLB}_{\text{CA}}(R) = \frac{c^2}{4} \cdot \frac{\Gamma_{\text{CA}} \left[\frac{(2N_U)(2M-1)}{36} - \frac{(N_U-1)(M-1)}{16} \right]}{(\Delta f^1)^2 (Q+1)^2 (N-1)}, \quad (62)$$

$$\text{CRLB}_{\text{CA}}(v_0) = \frac{c^2}{4} \cdot \frac{\Gamma_{\text{CA}} \left[\frac{(2N_U)(2N-1)}{36} - \frac{(N_U-1)(N-1)}{16} \right]}{(2f_C^1 T^1)^2 (M-1)}. \quad (63)$$

V. SIMULATION RESULTS AND ANALYSIS

In this section, the simulation results are provided to verify the high-speed communication and high-accuracy sensing capabilities of the proposed CA-enabled MIMO-OFDM ISAC system. Simulation parameters are detailed in Table II. The simulation results are obtained with 1000 times Monte Carlo simulations.

A. Performance of Communication

According to (43) and (46) derived in Section IV-A, the communication MIs of CA-enabled MIMO-OFDM ISAC system and MIMO-OFDM ISAC system under various SNR and N_U are simulated in Fig. 5.

In Fig. 5, the communication MI of the CA-enabled MIMO-OFDM ISAC signal is larger than that of the MIMO-OFDM ISAC signal under different N_U .

B. Performance of Sensing

In this section, the CRLBs and RMSEs of range and velocity estimations are simulated to demonstrate the high-accuracy sensing performance of the proposed CA-enabled MIMO-OFDM ISAC system.

1) *CRLB:* According to the closed-form sensing CRLBs derived in Section IV-B, the CRLBs for range and velocity estimations of CA-enabled MIMO-OFDM ISAC signal, MIMO-OFDM ISAC signal, and OFDM ISAC signal are simulated, as shown in Figs. 6 and 7. Fig. 6 reveals the following phenomena.

- The CRLB of the CA-enabled MIMO-OFDM ISAC signal is the lowest, indicating that the proposed CA-enabled

$$\Gamma_{CA} = \frac{1}{\varpi(2\pi)^2 M N N_U} \times \frac{1}{\frac{(2N_U-1)}{6} \frac{(2N-1)}{6} \frac{(2M-1)}{6} + (N_U-1) \left[\frac{(N-1)(M-1)}{32} - \frac{(M-1)(2N-1)}{96} - \frac{(N-1)(2M-1)}{96} \right] - \left(\frac{(M-1)(N-1)}{16} \right) \left(\frac{(2N_U-1)}{6} \right)}. \quad (61)$$

TABLE II: Simulation parameters [7], [29], [30].

Symbol	Parameter	Value	Symbol	Parameter	Value
f_C^1	Carrier frequency of low-frequency band	5.9 GHz [7]	f_C^2	Carrier frequency of high-frequency band	24 GHz [7]
M_1	Number of OFDM symbols on low-frequency band	64	M_2	Number of OFDM symbols on high-frequency band	64
N_1	Number of subcarriers on low-frequency band	512	N_2	Number of subcarriers on high-frequency band	512
T^1	Total symbol duration on low-frequency band	39.5 μ s	T^2	Total symbol duration on high-frequency band	9.7 μ s
Δf^1	Subcarrier spacing on low-frequency band	30 kHz [30]	Δf^2	Subcarrier spacing on high-frequency band	120 kHz [30]
N_T	Number of transmit antenna of BS	4	N_R	Number of received antenna of BS	4
N_U	Number of received antenna of UE	{4, 5, 6}	θ_{Rx}, θ_{Tx}	AoA and AoD of target	30°
r_0	Range of target	117 m	v_0	Velocity of target	13 m/s

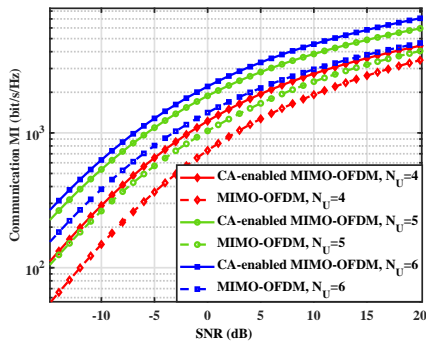


Fig. 5: Communication MI of the proposed CA-enabled MIMO-OFDM ISAC system and MIMO-OFDM ISAC system.

MIMO-OFDM ISAC signal has better range estimation performance than MIMO-OFDM ISAC signal and OFDM ISAC signal.

- Comparing with the CRLB of low-frequency MIMO-OFDM ISAC signal, the CRLB of high-frequency MIMO-OFDM ISAC signal is lower, which is caused by the large bandwidth resources of high-frequency signal.
- Comparing with the CRLB of OFDM ISAC signal, the CRLB of MIMO-OFDM ISAC signal is lower, which benefits from the spatial diversity of MIMO.

Fig. 7 demonstrates the following phenomena.

- The CRLB of CA-enabled MIMO-OFDM ISAC signal is lowest, indicating that the CA-enabled MIMO-OFDM ISAC signal has better performance of velocity estimation than MIMO-OFDM ISAC signal and OFDM ISAC signal.
- Upon observing Fig. 7(b), the high-frequency MIMO-OFDM ISAC signal and low-frequency MIMO-OFDM ISAC signal are overlapped, which also exist in the OFDM ISAC signals. The reason is as follows. According to (63), for the ISAC signals occupying the same number

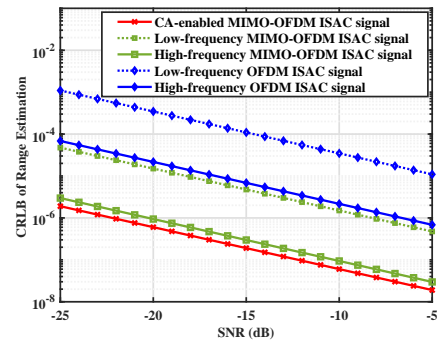


Fig. 6: Comparison of CRLB for range estimation

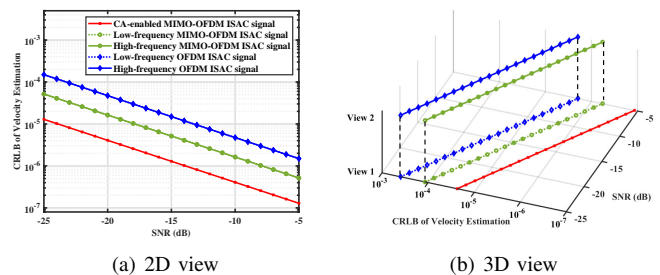


Fig. 7: Comparison of CRLB for velocity estimation

- of REs and satisfying $f_C^1 T^1 = f_C^2 T^2$ in simulation parameters, the CRLBs of velocity estimation are identical.
- Comparing with the CRLB of OFDM ISAC signal, the CRLB of MIMO-OFDM ISAC signal is lower, which also benefits from the spatial diversity of MIMO.

Therefore, the simulation results indicate the superior sensing performance of the proposed CA-enabled MIMO-OFDM ISAC signal compared with MIMO-OFDM ISAC signal and OFDM ISAC signal.

2) *RMSE*: The data-level and signal-level fusion methods are compared in Fig. 8, where the the following phenomena

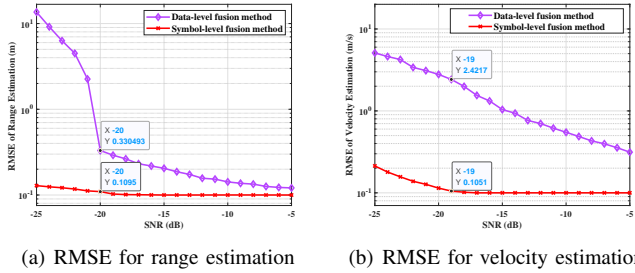


Fig. 8: Comparison of data-level fusion and symbol-level sensing data fusion methods

are revealed.

- In Fig. 8, the RMSE of symbol-level fusion method is consistently lower than that of the data-level fusion method, indicating the superiority of the proposed symbol-level fusion method over the data-level fusion method.
- Compared with the data-level fusion method, the accuracy of range and velocity estimations under symbol-level fusion method is improved by up to 66.91% and 95.67%, respectively.

Then, the RMSEs for range and velocity estimations of the proposed CA-enabled MIMO-OFDM ISAC signal and MIMO-OFDM ISAC signal are simulated in Fig. 9. There are several assumptions.

- 1) The SNR in the simulation is the transmit SNR of single RE.
- 2) The theoretical RMSEs of range and velocity estimations are expressed in (64) and (65), respectively [31].

$$\sigma_R = \frac{c}{2B\sqrt{2\chi}}, \quad (64)$$

$$\sigma_V = \frac{c}{2M_{\text{ofdm}}f_C T_C \sqrt{2\chi}}, \quad (65)$$

where B and χ are the bandwidth and received SNR of signal, respectively; M_{ofdm} is the number of OFDM symbols and f_C is the carrier frequency; T_C is the total symbol duration.

Fig. 9(a) reveals the following phenomena.

- With the increase of SNR, the RMSEs of CA-enabled MIMO-OFDM ISAC signal and MIMO-OFDM ISAC signal are stable, because the accuracy of sensing method is limited by the grid size.
- Comparing with the RMSEs of MIMO-OFDM ISAC signals, the RMSE of CA-enabled MIMO-OFDM ISAC signal is lower, indicating the superior performance of range estimation of the proposed CA-enabled MIMO-OFDM ISAC signal over the MIMO-OFDM ISAC signal.
- When SNR is smaller than -20 dB, comparing with the RMSE of low-frequency MIMO-OFDM ISAC signal, the RMSE of high-frequency MIMO-OFDM ISAC signal is higher. In the simulation, we employed a typical path loss model and set the received SNR of high-frequency signal 5 dB lower than that of low-frequency signal [32].

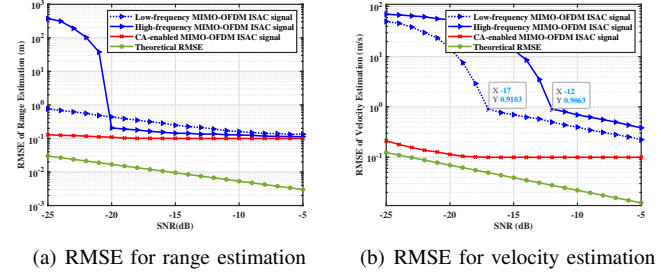


Fig. 9: Comparison of MIMO-OFDM ISAC signal on different frequency bands and CA-enabled MIMO-OFDM ISAC signal.

Therefore, for comparison under the same received SNR, the curve of high-frequency MIMO-OFDM ISAC signal needs to shift 5 dB to the left.

According to (65), since $f_C^1 T^1 = f_C^2 T^2$ in the simulation, the differences in the RMSEs of high and low frequency signals are only the received SNR.

VI. CONCLUSION

In this paper, CA-enabled MIMO-OFDM ISAC system is investigated, where CA aggregates fragmented high and low-frequency bands, achieving the high-speed communication and high-accuracy sensing. Firstly, we introduce the signal model of the proposed CA-enabled MIMO-OFDM ISAC system and the ISAC signal processing framework. To address the challenges in the sensing signal processing introduced by CA, symbol-level fusion method of the sensing data on high and low-frequency bands is proposed. In the proposed symbol-level fusion method, the phase alignment of the echo signals on high and low-frequency bands is realized by the angle compensation, space-domain diversity and vector cross-correlation operations. Then, the fusion algorithms of feature vectors are proposed to realize high-accuracy sensing. The simulation results reveal that the performance of symbol-level fusion method is better than that of data-level fusion method. Furthermore, the closed-form communication MI and sensing CRLB of the proposed ISAC signal are derived. Numerical results reveal that the proposed CA-enabled MIMO-OFDM ISAC signal exhibits superior communication rate and high-accuracy sensing performance over the conventional MIMO-OFDM ISAC signal. This work reveals the potential of CA-enabled MIMO-OFDM ISAC signal in enhancing communication and sensing capabilities.

APPENDIX A PROOF OF THEOREM 3

According to (12), the received echo signal by the p -th received antenna on the n -th subcarrier during the m -th OFDM symbol time is expressed as

$$y_{p,m,n} = A e^{j2\pi m f_C^b T^b \gamma} e^{-j2\pi n \Delta f^b \tau_0} e^{j2\pi p \left(\frac{d_r}{\lambda^b}\right) \sin \theta_{R_x}} + w_{p,m,n}, \quad (66)$$

where $A \in \mathbb{C}$ and $w_{p,m,n} \sim \mathcal{CN}(0, \sigma^2)$ is the AWGN.

The likelihood function for the joint estimation of $\sin \theta_{\text{Rx}}$, τ_0 , and γ is

$$\begin{aligned} \ln f(y; \sin \theta_{\text{Rx}}, \tau_0, \gamma) &= -\frac{M_b N_b N_U}{2} \ln(2\pi\sigma^2) \\ &\quad - \frac{1}{2\sigma^2} \sum_p \sum_m \sum_n (y_{p,m,n} - s_{p,m,n})^* (y_{p,m,n} - s_{p,m,n}), \end{aligned} \quad (67)$$

where the PDF is

$$\begin{aligned} f(y; \sin \theta_{\text{Rx}}, \tau_0, \gamma) &= \frac{1}{(2\pi\sigma^2)^{M_b N_b N_U/2}} e^{-\frac{1}{2\sigma^2} \sum_p \sum_m \sum_n |y_{p,m,n} - s_{p,m,n}|^2}, \end{aligned} \quad (68)$$

with

$$s_{p,m,n} = A e^{j2\pi m f_c T^b} \gamma e^{-j2\pi n \Delta f^b \tau_0} e^{j2\pi p \left(\frac{d}{\lambda b}\right) \sin \theta_{\text{Rx}}}. \quad (69)$$

Based on the relationship between the Fisher information matrix (FIM) and CRLB, we can obtain that

$$\begin{aligned} \mathbf{F}^{-1} &= \begin{bmatrix} F_{\sin \theta_{\text{Rx}}, \sin \theta_{\text{Rx}}} & F_{\sin \theta_{\text{Rx}}, \tau_0} & F_{\sin \theta_{\text{Rx}}, \gamma} \\ F_{\tau_0, \sin \theta_{\text{Rx}}} & F_{\tau_0, \tau_0} & F_{\tau_0, \gamma} \\ F_{\gamma, \sin \theta_{\text{Rx}}} & F_{\gamma, \tau_0} & F_{\gamma, \gamma} \end{bmatrix}^{-1} \\ &= \begin{bmatrix} CRLB(\sin \theta_{\text{Rx}}) & Cov(\sin \theta_{\text{Rx}}, \tau_0) & Cov(\sin \theta_{\text{Rx}}, \gamma) \\ Cov(\tau_0, \sin \theta_{\text{Rx}}) & CRLB(\tau_0) & Cov(\tau_0, \gamma) \\ Cov(\gamma, \sin \theta_{\text{Rx}}) & Cov(\gamma, \tau_0) & CRLB(\gamma) \end{bmatrix}, \end{aligned} \quad (70)$$

where $Cov(\cdot)$ is the covariance operation and $F_{\alpha, \beta} = -E \left[\frac{\partial^2 \ln f(x; \alpha, \beta, \dots)}{\partial \alpha \partial \beta} \right]$.

According to (67) and (70), the CRLBs of angle, range, and velocity estimations for MIMO-OFDM ISAC system are derived, as shown in **Theorem 3**.

REFERENCES

- [1] M. Deng, Z. Yao, X. Li, H. Wang, A. Nallanathan, and Z. Zhang, "Dynamic multi-objective AWPSO in DT-assisted UAV cooperative task assignment," *IEEE J. Sel. Areas Commun.*, Aug 2023.
- [2] Z. Wang and V. W. Wong, "Deep Learning for ISAC-Enabled End-to-End Predictive Beamforming in Vehicular Networks," in *IEEE Int. Conf. Commun.* IEEE, Oct 2023, pp. 5713–5718.
- [3] K. Meng, Q. Wu, S. Ma, W. Chen, K. Wang, and J. Li, "Throughput Maximization for UAV-Enabled Integrated Periodic Sensing and Communication," *IEEE Trans. Wireless Commun.*, vol. 22, no. 1, pp. 671–687, Aug 2023.
- [4] Z. Du, F. Liu, W. Yuan, C. Masouros, Z. Zhang, S. Xia, and G. Caire, "Integrated Sensing and Communications for V2I Networks: Dynamic Predictive Beamforming for Extended Vehicle Targets," *IEEE Trans. Wireless Commun.*, vol. 22, no. 6, pp. 3612–3627, Nov 2023.
- [5] Z. Wei, H. Liu, Z. Feng, H. Wu, F. Liu, and Q. Zhang, "Deep Cooperation in ISAC System: Resource, Node and Infrastructure Perspectives," *arXiv preprint arXiv:2403.02565*, 2024.
- [6] K. I. Pedersen, F. Frederiksen, C. Rosa, H. Nguyen, L. G. U. Garcia, and Y. Wang, "Carrier aggregation for LTE-advanced: functionality and performance aspects," *IEEE Commun. Mag.*, vol. 49, no. 6, pp. 89–95, Jun 2011.
- [7] Z. Wei, H. Liu, X. Yang, W. Jiang, H. Wu, X. Li, and Z. Feng, "Carrier Aggregation Enabled Integrated Sensing and Communication Signal Design and Processing," *IEEE Trans. Veh. Tech.*, vol. 73, no. 3, pp. 3580–3596, Mar 2024.
- [8] C. Pfeffer, R. Feger, and A. Stelzer, "A stepped-carrier 77-GHz OFDM MIMO radar system with 4 GHz bandwidth," in *IEEE EuRAD Conf.* IEEE, Dec 2015, pp. 97–100.
- [9] B. Schweizer, C. Knill, D. Schindler, and C. Waldschmidt, "Stepped-carrier OFDM-radar processing scheme to retrieve high-resolution range-velocity profile at low sampling rate," *IEEE Trans. Microwave Theory Tech.*, vol. 66, no. 3, pp. 1610–1618, Sep 2017.
- [10] Y. Huang, D. Huang, Q. Luo, S. Ma, S. Hu, and Y. Gao, "NC-OFDM RadCom system for electromagnetic spectrum interference," in *IEEE Int. Conf. Commun. Tech.* IEEE, 2017, pp. 877–881.
- [11] H. Liu, Z. Wei, F. Li, Y. Lin, H. Qu, H. Wu, and Z. Feng, "Integrated Sensing and Communication Signal Processing Based On Compressed Sensing Over Unlicensed Spectrum Bands," *IEEE Trans. Cognit. Commun. Networking*, Apr 2024.
- [12] K. M. Cuomo, "A bandwidth extrapolation technique for improved range resolution of coherent radar data. revision 1," Massachusetts Inst of Tech Lexington Lincoln Lab, Tech. Rep., Dec 1992.
- [13] K. Suwa and M. Iwamoto, "Bandwidth extrapolation technique for polarimetric radar data," *IEICE Trans. Commun.*, vol. 87, no. 2, pp. 326–334, Feb 2004.
- [14] M. Hua, Q. Wu, W. Chen, and A. Jamalipour, "Integrated sensing and communication: Joint pilot and transmission design," *arXiv preprint arXiv:2211.12891*, 2022.
- [15] F. Liu, C. Masouros, A. Li, H. Sun, and L. Hanzo, "MU-MIMO Communications With MIMO Radar: From Co-Existence to Joint Transmission," *IEEE Trans. Wireless Commun.*, vol. 17, no. 4, pp. 2755–2770, Apr 2018.
- [16] X. Hu, C. Masouros, F. Liu, and R. Nissel, "Low-PAPR DFRC MIMO-OFDM Waveform Design for Integrated Sensing and Communications," in *IEEE Int. Conf. Commun.*, Aug 2022, pp. 1599–1604.
- [17] Z. Xiao, R. Liu, M. Li, and Q. Liu, "A Novel Joint Angle-Range-Velocity Estimation Method for MIMO-OFDM ISAC Systems," *arXiv preprint arXiv:2308.03387*, 2023.
- [18] P. Aggarwal and V. A. Bohara, "Analytical Characterization of Dual-Band Multi-User MIMO-OFDM System With Nonlinear Transmitter Constraints," *IEEE Trans. Commun.*, vol. 66, no. 10, pp. 4536–4549, May 2018.
- [19] Y. S. Cho, J. Kim, W. Y. Yang, and C. G. Kang, *MIMO-OFDM wireless communications with MATLAB*. John Wiley & Sons, 2010.
- [20] Y. Guo, Y. Liu, Q. Wu, X. Li, and Q. Shi, "Joint Beamforming and Power Allocation for RIS Aided Full-Duplex Integrated Sensing and Uplink Communication System," *IEEE Trans. Wireless Commun.*, pp. 1–1, Oct 2023.
- [21] Z. Xu and A. Petropulu, "A bandwidth efficient dual-function radar communication system based on a MIMO radar using OFDM waveforms," *IEEE Trans. Signal Process.*, vol. 71, pp. 401–416, Feb 2023.
- [22] R. Schmidt, "Multiple emitter location and signal parameter estimation," *IEEE Trans. Antennas Propag.*, vol. 34, no. 3, pp. 276–280, Mar 1986.
- [23] Z. Wei, R. Xu, Z. Feng, H. Wu, N. Zhang, W. Jiang, and X. Yang, "Symbol-level integrated sensing and communication enabled multiple base stations cooperative sensing," *IEEE Trans. Veh. Tech.*, pp. 1–15, Aug 2023.
- [24] M. Braun, C. Sturm, A. Niethammer, and F. K. Jondral, "Parametrization of joint OFDM-based radar and communication systems for vehicular applications," in *2009 IEEE 20th International Symposium on Personal, Indoor and Mobile Radio Communications*, Apr 2009, pp. 3020–3024.
- [25] Z. Wei, F. Li, H. Liu, X. Chen, H. Wu, K. Han, and Z. Feng, "Multiple Reference Signals Collaborative Sensing for Integrated Sensing and Communication System Towards 5G-A and 6G," *arXiv preprint arXiv:2312.02170*, 2023.
- [26] C. Ouyang, Y. Liu, H. Yang, and N. Al-Dhahir, "Integrated sensing and communications: A mutual information-based framework," *IEEE Commun. Mag.*, vol. 61, no. 5, pp. 26–32, May 2023.
- [27] Z. Wei, J. Piao, X. Yuan, H. Wu, J. A. Zhang, Z. Feng, L. Wang, and P. Zhang, "Waveform Design for MIMO-OFDM Integrated Sensing and Communication System: An Information Theoretical Approach," *IEEE Trans. Commun.*, vol. 72, no. 1, pp. 496–509, Sep 2024.
- [28] H. Hua, T. X. Han, and J. Xu, "MIMO Integrated Sensing and Communication: CRB-Rate Tradeoff," *IEEE Trans. Wireless Commun.*, vol. 23, no. 4, pp. 2839–2854, Aug 2024.
- [29] M. Braun, C. Sturm, A. Niethammer, and F. K. Jondral, "Parametrization of joint ofdm-based radar and communication systems for vehicular applications," in *2009 IEEE 20th International Symposium on Personal, Indoor and Mobile Radio Communications*. IEEE, Apr 2009, pp. 3020–3024.
- [30] 3GPP, "NR; Physical channels and modulation," *3rd Generation Partnership Project (3GPP), Technical Specification (TS) 38.211*, vol. 9, 2018.
- [31] M. I. Skolnik, "Theoretical accuracy of radar measurements," *IRE Transactions on Aeronautical and Navigational Electronics*, no. 4, pp. 123–129, Dec 1960.
- [32] A. Goldsmith, *Wireless communications*. Cambridge university press, 2005.